Article

Exploring the dynamic evolution of lattice oxygen on exsolved-Mn_2O_3@$SmMn_2O_5$ interfaces for NO Oxidation

Xiyang Wang [1,2,7], Qilei Yang[1,7], Xinbo Li[3], Zhen Li [1], Chuan Gao[1], Hui Zhang [4], Xuefeng Chu[1], Carl Redshaw[5], Shucheng Shi [6], Yimin A. Wu [2], Yongliang Ma[1], Yue Peng [1] ✉, Junhua Li [1] & Shouhua Feng [3]

Lattice oxygen in metal oxides plays an important role in the reaction of diesel oxidation catalysts, but the atomic-level understanding of structural evolution during the catalytic process remains elusive. Here, we develop a Mn_2O_3/$SmMn_2O_5$ catalyst using a non-stoichiometric exsolution method to explore the roles of lattice oxygen in NO oxidation. The enhanced covalency of Mn–O bond and increased electron density at Mn^{3+} sites, induced by the interface between exsolved Mn_2O_3 and mullite, lead to the formation of highly active lattice oxygen adjacent to Mn^{3+} sites. Near-ambient pressure X-ray photo-electron and absorption spectroscopies show that the activated lattice oxygen enables reversible changes in Mn valence states and Mn-O bond covalency during redox cycles, reducing energy barriers for NO oxidation and promoting NO_2 desorption via the cooperative Mars-van Krevelen mechanism. Therefore, the Mn_2O_3/$SmMn_2O_5$ exhibits higher NO oxidation activity and better resistance to hydrothermal aging compared to a commercial Pt/Al_2O_3 catalyst.

Considering the high fuel efficiencies, diesel engines are prominently utilized in heavy-duty vehicles, construction equipment and industrial machinery etc[1,2]. The diesel oxidation catalyst (DOC), integral in these applications, is used to oxidize CO and hydrocarbons to CO_2, as well as also converting emitted NO to NO_2 during NO oxidation[2–4]. Where the produced NO_2, possessing higher oxidation ability than O_2, is used to oxidize the soot in the back-end diesel particulate filters at low temperatures, making it a key performance indicator of DOCs[5,6]. Conventionally, Pt-based catalysts are used as commercial DOCs, yet they face substantial drawbacks including cost and sintering issues[6–9]. Hence, the thrust towards Pt-free catalysts with good thermal stability such as mullites (AB_2O_5) is gaining much attention as one of the next-generation DOCs to meet the increasingly stringent regulations in the US, EU etc[10–13]. Despite the significant progress achieved in NO

oxidation on metal-oxide catalysts, the dynamic evolution mechanism of mullite catalysts remains enigmatic.

Over the past few decades, it has been generally believed that NO oxidation on metal oxides is catalyzed solely by surface cations, following the Eley-Rideal (E-R) mechanism. To enhance the catalytic performance, traditional improvement strategies focused on the secondary metal doping modifications in the valence state of the surface metal sites[14,15] and in decomposition of nitrate or nitrite species on catalysts[16,17]. Wang et al.[2] demonstrated that a Sr-doped mullite exhibits even higher activity for NO oxidation compared to a commercial Pt/Al_2O_3 (87% versus 55% NO conversion at 300 °C). The good activity was attributed to an increased formation of nitrates at surface-exposed Mn^{4+} sites, which allowed for facile decomposition to NO_2. However, recent results challenged the notion that metal or surface cation sites

[1]School of Environment, Tsinghua University, Beijing, PR China. [2]Department of Mechanical and Mechatronics Engineering, Waterloo Institute for Nano-technology, Materials Interface Foundry, University of Waterloo, Waterloo, ON, Canada. [3]State Key Laboratory of Inorganic Synthesis and Preparative Chemistry, College of Chemistry, Jilin University, Changchun, PR China. [4]State Key Laboratory of Functional Materials for Informatics, Shanghai Institute of Microsystem and Information Technology, Chinese Academy of Sciences, Shanghai, PR China. [5]Chemistry, School of Natural Sciences, University of Hull, Hull, UK. [6]School of Physical Science and Technology, Shanghai Tech University, Shanghai, PR China. [7]These authors contributed equally: Xiyang Wang, Qilei Yang. ✉e-mail: pengyue83@tsinghua.edu.cn

alone are responsible for catalytic activity[3,8,18]. It has been found that surface lattice oxygen (O_{latt}) of metal oxides can directly participate in some redox reactions. For instance, surface oxygen exchange kinetics in solid oxide fuel cells[19,20], oxygen evolution in water splitting[21–23], and lithium storage capacity in batteries[24–26]. In addition, the introduction of oxygen vacancies[27–29] or the doping of isovalent A/B-site cations in metal oxides[29–31] can also enhance the oxidation ability with/without varying the valence state of metal sites. Our previous work also indirectly pointed out that removing inactive Sm ions of a mullite catalyst surface could enhance the covalency of the Mn−O bond, improve the lattice oxygen activity, and exposed more Mn^{4+} ions to facilitate the decomposition of nitrate species[16,17], but the detailed roles and mechanism of lattice oxygen during NO oxidation remained elusive due to the interference of Mn^{4+} ions and the E-R mechanism. Recent density functional theory (DFT) calculations suggested that surface lattice oxygen on metal oxides may serve as exceptionally active sites in NO oxidation, with lower energy barriers in NO oxidation compared to traditional metal sites[10,32–34]. Zheng et al. theoretically unraveled the cooperative Mars-van Krevelen (MvK) mechanism on the O_{latt} sites around Mn^{3+} ions and the nitrite intermediates[10], enhancing the understanding of O_{latt} sites in metal oxide catalysts during NO oxidation. However, the dynamic structure evolutions of cations and O_{latt} sites during real-time reactions are poorly understood because of the limited direct experimental evidence in monitoring the reaction process[35]. The methodology of in-situ technologies is essential to address this knowledge gap and promote the clarification of chemical descriptors (for example, valence state, bond covalency, electron density, etc.) and reaction mechanisms at the atomic level.

In this study, we provide insights into the underlying active sites of traditional mullite $SmMn_2O_5$ (SMO) and $Mn_2O_3/SmMn_2O_5$ (Mn_2O_3/SMO) catalysts with exsolved-Mn_2O_3 on the SMO surface via the non-stoichiometric exsolution method. Leveraging an array of near ambient pressure X-ray photoelectron/absorption spectroscopies (*NAP-XPS* and *NAP-XAS*), we directly observed that the NO oxidation process on Mn_2O_3/SMO relies on the dynamic covalency variations of the Mn-O bond at O_{latt} adjacent to the Mn^{3+} cations. Unlike the E-R mechanism occurring at Mn^{4+} sites, the O_{latt} of Mn_2O_3/SMO predominantly follows the cooperative MvK mechanism, and the induced O_{latt}-NO_2 nitrite species facilitates the NO_2 desorption. This work identifies the O_{latt} as the active site both theoretically and experimentally, and further sheds light on the mechanism of NO oxidation.

Results

### Structure of the catalyst interface

The Mn_2O_3/SMO catalyst was prepared by the nonstoichiometric exsolution method. During a high-temperature calcination (800 °C), a surplus of MnO_x was accumulated on the mullite (SMO) surface and transitioned into a stable Mn_2O_3 phase. Pristine SMO, Mn_2O_3, and the co-impregnated sample of Mn_2O_3 on SMO (Mn_2O_3-SMO) were synthesized and calcined at 800 °C[16,17]. The X-ray diffraction (XRD) results depicted confirm that the Mn_2O_3/SMO possesses a mullite structure whilst further containing an exsolved-Mn_2O_3 phase at 32.9° (Fig. 1a). The main diffraction peak (211) of Mn_2O_3/SMO exhibits an obvious shift compared to that of SMO and Mn_2O_3-SMO (Supplementary Fig. 1), suggesting the lattice contraction occurs on the mullite support of Mn_2O_3/SMO. The refined XRD results of SMO and Mn_2O_3/SMO (Supplementary Fig. 2 and Supplementary Table 1) also demonstrate that the lattice constant and unit cell volume parameter of SMO change from $a = 7.44$ Å ($V = 363.53$ Å) to $a = 7.43$ Å of Mn_2O_3/SMO ($V = 362.6$ Å). Such a lattice contraction is mainly attributed to the produced oxygen vacancies and interface interactions.

The interface atomic structure was imaged utilizing high-angle annular dark field scanning transmission electron microscopy (HAADF-STEM), revealing that the spacings of the lattice fringe on the SMO sample are 3.46 and 2.93 Å, assignable to the (102) and (200)

facets of mullite, respectively (Fig. 1b and Supplementary Figs. 3–4). It is interesting to note that the spacing on the Mn_2O_3/SMO is 3.63 Å, assignable to the (020) facet of mullite (Fig. 1b, c), coherently aligning with the peak shift in the XRD results. The spacings of the lattice fringe on the exsolved oxide region can be allocated to the ($\bar{2}00$) and (222) facets of the Mn_2O_3 phase. The electron energy loss spectroscopy (EELS) reveals intricate details about the local electronic structure of catalysts. Mn L-edge EELS spectra (Fig. 1d) show that the Mn_2O_3/SMO contains more Mn^{3+} cations and lower shifts for peak positions than does Mn_2O_3-SMO at the interface and mullite regions, but a single SMO surface exists with the same Mn valence states and peak positions with mullite regions of Mn_2O_3-SMO. These results directly imply that the exsolved Mn_2O_3/SMO possesses strong interface interactions while there is a negligible interfacial interaction on Mn_2O_3-SMO. The Mn L-edge EELS results highlight that the conventional impregnation method can only present a slight impact on the electronic structure between Mn_2O_3 and SMO. However, the interface between exsolved-Mn_2O_3 and SMO of Mn_2O_3/SMO presents an important electron enrichment on Mn atoms, which is a prerequisite for generating a robust electron transfer at the interface. Furthermore, O K-edge EELS spectra reveal that the Mn-O bond covalency at the SMO surface of exsolved Mn_2O_3/SMO is stronger than mullite and the deposited Mn_2O_3-SMO due to the higher energy position for the adsorption peak of the Mn-O bond (Supplementary Fig. 5). While both SMO and Mn_2O_3-SMO show the same covalency of Mn-O bond because of the same peak position. These results demonstrate the interface interactions and the activation of lattice oxygen in exsolved Mn_2O_3/SMO. A schematic representation of the electron transfer at the interface (Fig. 1e) reveals that the electron transfer from exsolved Mn_2O_3 to SMO activates the O_{latt} sites of Mn_2O_3/SMO.

The H_2 temperature programmed reduction (H_2-TPR) profiles (Supplementary Fig. 6) infer that the Mn^{4+} of Mn_2O_3/SMO exhibits a slightly lower reduction peak at 410 °C than the other samples, suggesting its high reducibility. The O_2 temperature programmed desorption (O_2-TPD) profiles (Supplementary Fig. 7) manifest that Mn_2O_3/SMO possesses more adsorbed oxygen species below 180 °C and the considerable amount of active surface O_{latt} occurring at 180–300 °C. The NO temperature programmed desorption (NO-TPD) profiles (Supplementary Fig. 8) display a lower temperature for NO_x desorption at 150 °C on Mn_2O_3/SMO. The above results confirm that the interface between exsolved-Mn_2O_3 and the mullite support of Mn_2O_3/SMO can improve the reducibility of surface Mn and the number of O_{latt}, enhancing the NO_x desorption ability at low temperatures.

Mn K-edge X-ray absorption near edge structure (XANES) and extended X-ray absorption fine (EXAFS) spectroscopies reveal that the Mn_2O_3/SMO possesses the same average valence state of bulk Mn atoms with Mn_2O_3-SMO due to the similar adsorbed edge position and exhibits a shorter Mn−O bond length compared to Mn_2O_3-SMO and SMO (Fig. 1f and Supplementary Figs. 9, 10). This result demonstrates the important effect of the exsolved interface on tuning the Mn coordination environment and surface electronic state because the average valence of the bulk Mn atom has little relevance with the interface. Furthermore, the Sm L_3-edge XANES spectra (Fig. 1g) demonstrate that Mn_2O_3/SMO possesses a weaker intensity of white line peak than Mn_2O_3-SMO and SMO, resulting in an increased number of electrons at the Sm sites. The consequential electron transfer and ensuing modifications are further confirmed by a shift in the Sm $3d$ spectra of X-ray photoelectron spectroscopy (*XPS*) (Fig. 1h). With respect to the Mn L-edge *XAS* spectra (Supplementary Fig. 11), Mn_2O_3/SMO presents a lower intensity of white line peak and a diminished peak intensity ratio of L_3/L_2 compared to SMO and Mn_2O_3-SMO, suggesting that the Mn_2O_3/SMO hosts surplus electrons in the Mn $3d$ orbitals. An exploration of O K-edge *XAS* spectra on Mn_2O_3/SMO indicates notable variations in Fig. 1i and Supplementary Fig. 12) a stronger white line peak; 2) more hybrid orbitals of Mn $3d$ and O $2p$; 3)
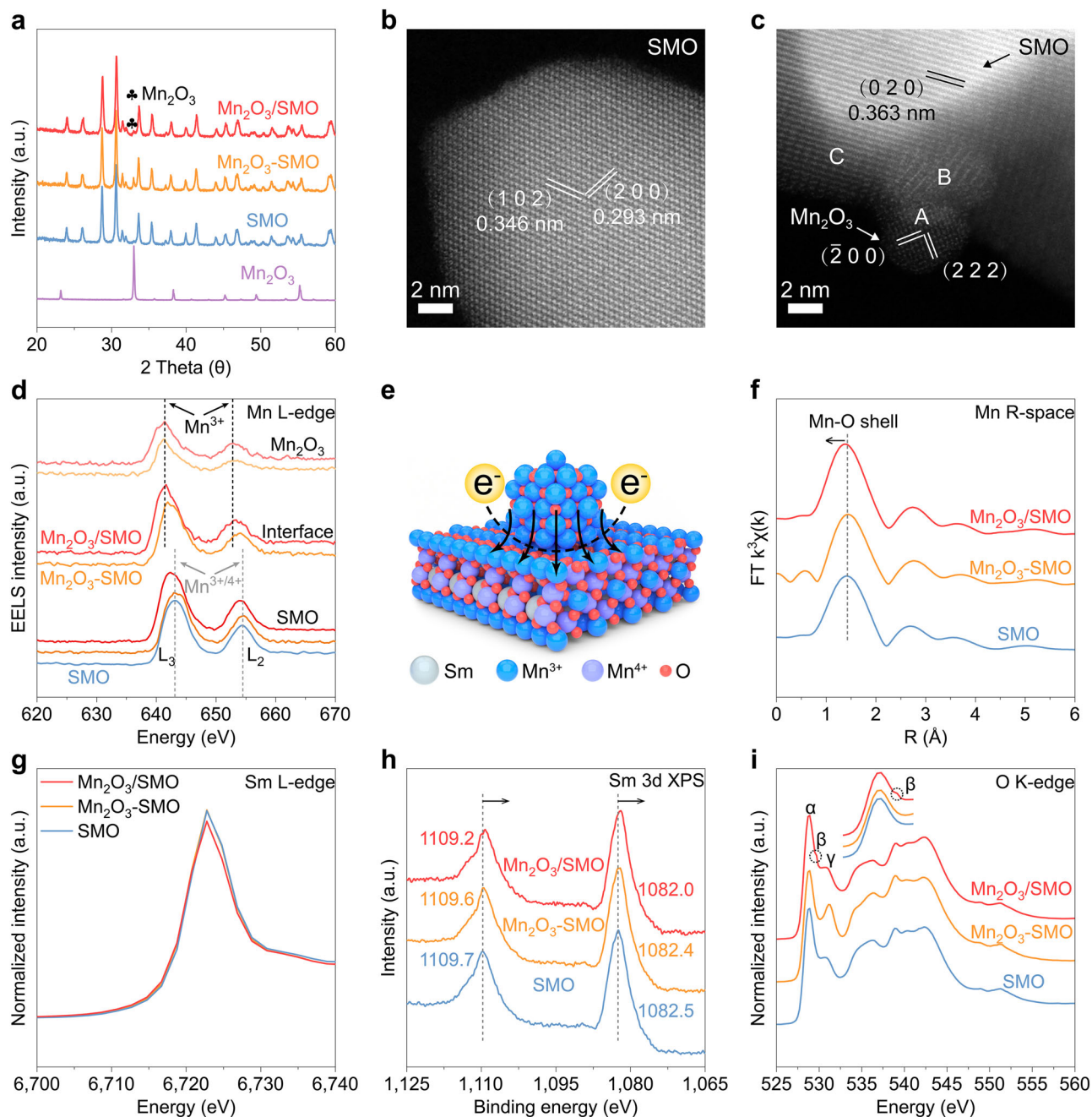
Fig. 1 | Surface and interface electronic structure characterizations. a The X-ray diffraction patterns; the high-angle annular dark-field scanning transmission electron microscopies (HAADF-STEM) of (**b**) $SmMn_2O_5$ (SMO) and (**c**) Mn_2O_3/$SmMn_2O_5$ (Mn_2O_3/SMO; A: SMO surface; B: interface; C: Mn_2O_3); (**d**) the normalized Mn L-edges electron energy loss spectroscopies (EELS) of SMO, Mn_2O_3-$SmMn_2O_5$ (Mn_2O_3-SMO), and Mn_2O_3/SMO at the position of A, B, and C; (**e**) Schematic illustration of the interface interactions on Mn_2O_3/SMO; (**f**) the R-space Fourier-transformed FT ($k^3\chi(k)$) of Mn K-edge (extended x-ray absorption fine structure) EXAFS spectra, (**g**) Sm L_3-edge (X-ray absorption near edge structure) XANES spectra, (**h**) Sm 3d XPS, and **i** the normalized O K-edge XANES spectra of SMO, Mn_2O_3-SMO, and Mn_2O_3/SMO.

a higher peak intensity ratio of α/γ obtained on Mn_2O_3/SMO, where the peaks α and γ represent the Mn 3d e_g/t_{2g} and e_g orbitals, respectively[36,37]. These Mn L-edge and O K-edge soft-*XAS* spectra analyses agree well with the Mn L-edge and O K-edge EELS spectra in surface and interface electronic structure of these samples. The EPR spectra further manifest that the exsolved Mn_2O_3/SMO possesses the most oxygen vacancies among these samples, which stems from the strong interface interactions (Supplementary Fig. 13).

These disparities indicate that Mn_2O_3/SMO displays a higher covalency of the Mn-O bond because of the strong orbital hybridizations of Mn 3d and O 2p. These observations are complemented by a comprehensive analysis to gain insights into the electronic structures at the interface between exsolved-M_2O_3 and SMO. Fundamentally, this interface facilitates effective electron transfer from the exsolved-Mn_2O_3 to SMO, enhancing the covalency of the Mn-O bond at the O_{latt} adjacent to the Mn^{3+} cations (Fig. 1e)[16,17,38].

NO oxidation performance

The NO conversions of Pt/Al_2O_3, SMO, Mn_2O_3/SMO, Mn_2O_3, and Mn_2O_3-SMO catalysts are conducted to analyze the catalytic performance (Fig. 2a). Distinctly paramount among these, the Mn_2O_3/SMO exhibits superior NO conversion (93%) at 270 °C. The T_{80} (the onsite
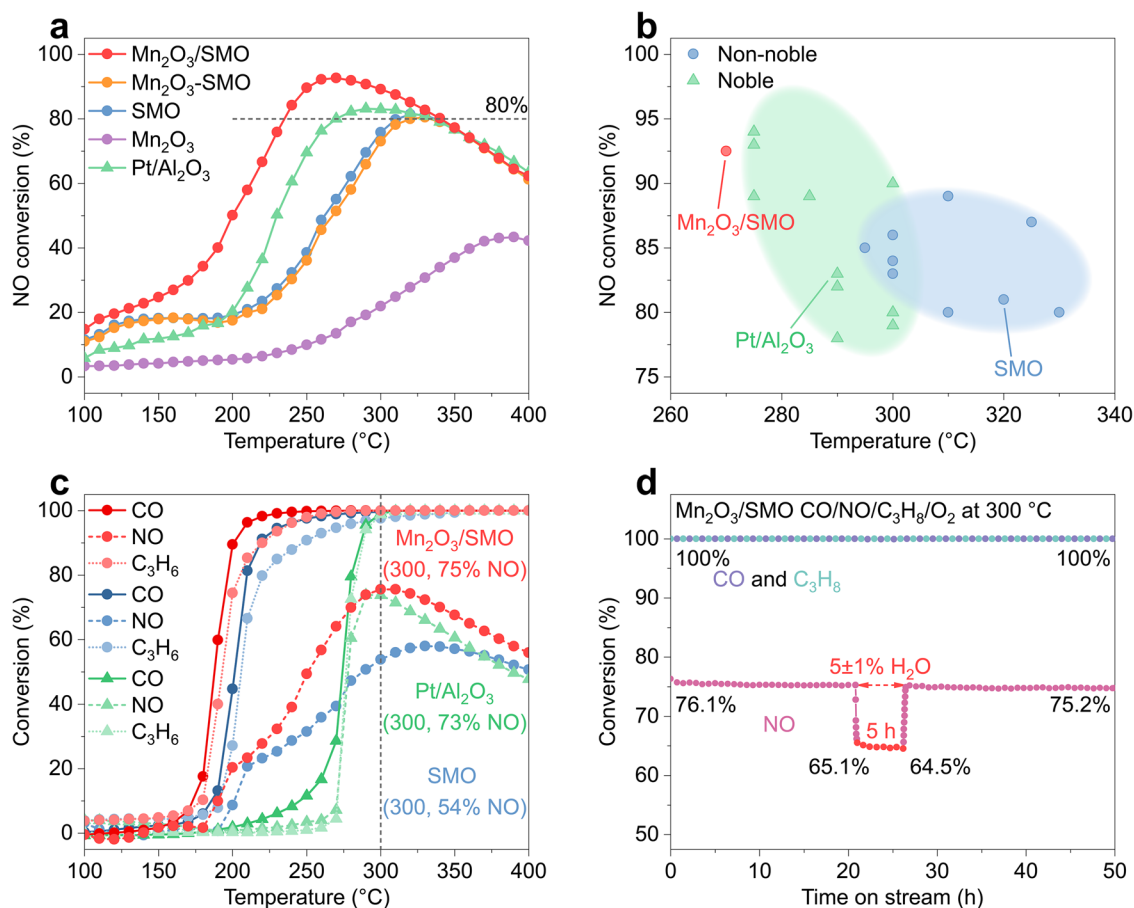
Fig. 2 | Oxidation activity of diesel exhaust gas. a NO oxidation activity of Pt/Al$_2$O$_3$, SmMn$_2$O$_5$ (SMO), Mn$_2$O$_3$, Mn$_2$O$_3$/SmMn$_2$O$_5$ (Mn$_2$O$_3$/SMO), and Mn$_2$O$_3$-SmMn$_2$O$_5$ (Mn$_2$O$_3$-SMO). **b** Plot of maximum conversion for NO oxidation vs. temperature for Mn$_2$O$_3$/SMO, mullite-based catalysts, perovskite-based catalysts, and noble metal catalysts. **c** Diesel oxidation catalyst (DOC) performance of SMO, Mn$_2$O$_3$/SMO, and Pt/Al$_2$O$_3$. **d** DOC stability of Mn$_2$O$_3$/SMO for long-term oxidation reaction at 300 °C. Reaction conditions: 500 ppm NO, 1% CO, 2000 ppm C$_3$H$_6$, 10% O$_2$, 5 ± 1% H$_2$O, and balance N$_2$.

temperature when NO conversion is higher than 80%) of Mn$_2$O$_3$/SMO (235 °C) is also 50 and 100 °C lower than that of the Pt/Al$_2$O$_3$ and Mn$_2$O$_3$-SMO samples. The activity profile of Mn$_2$O$_3$-SMO is quite similar to that of SMO. This finding underscores the critical roles of the exsolved interface, demonstrating that the exsolved Mn$_2$O$_3$ (Mn$_2$O$_3$/SMO) rather than the impregnated Mn$_2$O$_3$ (Mn$_2$O$_3$-SMO) improves the NO oxidation activity of SMO. To better understand the impact of exsolved Mn$_2$O$_3$ on NO oxidation, we have synthesized a variety of exsolved Mn$_2$O$_3$-supported samples with diverse Mn$_2$O$_3$ content. Incrementing the Mn$_2$O$_3$ content does not contribute much to the activity of NO oxidation (Supplementary Fig. 14). Combined with the results of structure characterizations, the active sites in Mn$_2$O$_3$/SMO are mainly at the surface/interface of the SMO and the key role of the Mn$_2$O$_3$ species is to tune the surface/interface electronic structure of the SMO. It is also discovered that Mn$_2$O$_3$/SMO maintains the greatest activity across the component range because of the higher interface oxygen defect concentrations. This provides a reasonable deduction that the main active sites of Mn$_2$O$_3$/SMO are located primarily at the interface instead of surface Mn$_2$O$_3$.

In order to obtain a comparative measurement of activity, a graph representing the correlation between maximum NO conversion and temperatures for previously reported catalysts (with/without noble metals) is summarized (Fig. 2b). Mn$_2$O$_3$/SMO still manifests a supreme performance as it functions at a substantially lower reaction temperature and demonstrates a higher maximum NO conversion compared to both noble metal[39–45] and transition metal-oxide

(perovskite[3,34,46] and mullite[2,17,27,30,47]) counterparts. In addition, we also tested the DOC performance in terms of CO, C$_3$H$_6$, and NO subjected to laboratory-simulated diesel exhaust conditions (Fig. 2c). Mn$_2$O$_3$/SMO still exhibits superior activities in the oxidations of CO, C$_3$H$_6$, and NO as compared to Pt/Al$_2$O$_3$ and Mn$_2$O$_3$-SMO[17]. Fig. 2d shows the higher durability and water vapor resistance (Supplementary Fig. 15) of Mn$_2$O$_3$/SMO in 50 h, as well as excellent thermal stability at 800 °C aging for 10 h (Supplementary Fig. 16). We have also coated the slurry of Mn$_2$O$_3$/SMO on a honeycomb Cordierite-support and tested its DOC performance (Supplementary Fig. 17). The DOC performance of the honeycomb samples can meet the DOC standards of China Environmental Protection Industry Association (T/CAEPI 12.1-2017). This reinforces the superior robustness and functionality of Mn$_2$O$_3$/SMO, as well as the simple preparation method, making it one a promising candidate as a DOC catalyst.

To further align with realistic operational conditions in diesel vehicles, a CO$_2$ concentration of around 8% and H$_2$O at around 8% as well as thermal aging resistance are necessary to pretreat the catalyst before evaluating the catalytic performance of SMO and Mn$_2$O$_3$/SMO (Supplementary Fig. 18)[48]. Mn$_2$O$_3$/SMO displays better catalytic activity for NO oxidation (71.8% conversion at 325 °C), CO oxidation (100% conversion at 300 °C), C$_3$H$_6$ oxidation (100% conversion at 300 °C) than SMO (100% CO and 99.4% C$_3$H$_6$ conversions at 300 °C and 58.1% NO conversion at 350 °C). The tested data demonstrate the application prospect of the exsolved Mn$_2$O$_3$/SMO catalyst for exhaust oxidation treatment. In addition, we also measured the DOC durability of the
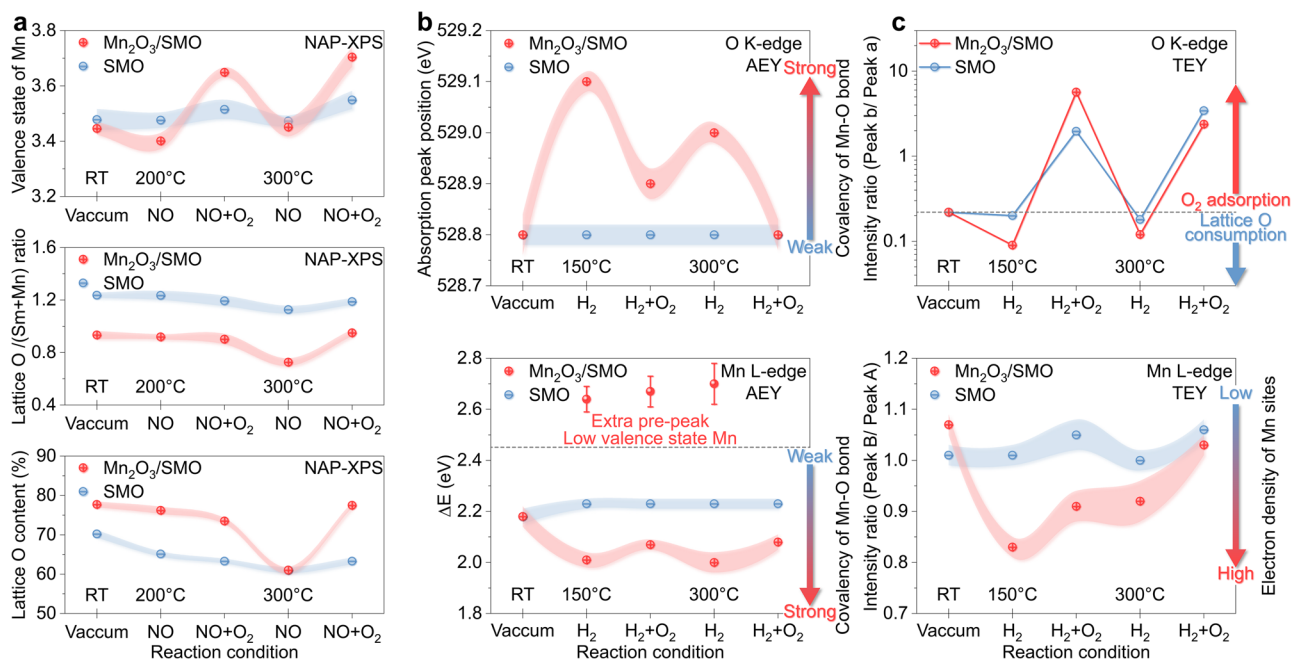
Fig. 3 | Dynamic structure evolutions of lattice O and metal Mn sites. a Dynamic evolutions of Mn valence state in *NAP-XPS* results, O_{latt}/(Sm+Mn) ratio and lattice oxygen (O_{latt}) content of $Mn_2O_3/SmMn_2O_5$ (Mn_2O_3/SMO) and $SmMn_2O_5$ (SMO) in NO oxidation; dynamic evolutions of covalency of the Mn-O bond and Mn *3d*

orbitals at the Mn sites of Mn_2O_3/SMO and SMO in *NAP-XAS* results of (**b**) AEY and (**c**) TEY modes. These error bars are mainly derived from fitting, reading, and random errors of experimental data.

exsolved Mn_2O_3/SMO catalyst for 64 h under the conditions of 8% CO_2 and 8% H_2O (Supplementary Fig. 19). 8% water vapor can decrease the catalytic oxidation property (56.9% NO conversion), which stems from the competitive adsorption of water vapor at the active sites. When water vapor is removed from reaction system, the catalytic activity of Mn_2O_3/SMO becomes better (73% NO conversion) and keeps the long-term durability for 15 h. Then, the 8% water vapor is pumped into the reactor again, the catalytic performance is the same as for the last water vapor condition (56.9% NO conversion). After removing the water vapor, the catalytic activity rapidly restores to the original level before secondly adding water vapor (73% NO conversion) and the system remains unchanged for the next 10 h. The initial tests of 20 h under NO, CO, C_3H_6, O_2, H_2O, CO_2, and N_2 belong to the pre-treatment process of catalysts. According to the standard practices of DOCs, these catalysts are aged at 750 °C for 50 h with 10% concentration of water vapor. After pretreatment, the catalytic oxidation reaction measurements of these aged catalysts are further conducted under the conditions of a large amount of water vapor (≥8%) and CO_2 (≥8%) (Supplementary Fig. 20). The exsolved Mn_2O_3/SMO shows the higher performance for NO, CO, and C_3H_6 oxidation than the SMO and commercial Pt/Al_2O_3. At 325 °C, CO, NO, and C_3H_6 conversions of the Mn_2O_3/SMO are 100%, 62.6%, and 100%, respectively.

Dynamic evolutions of O_{latt}-Mn^{3+} sites

In order to elucidate the dynamic evolutions of the valence state of Mn and reactivity of O_{latt} in NO oxidation, *NAP-XPS* spectra of Mn_2O_3/SMO and SMO were employed. The O *1s* and Mn *2p* XPS spectra of Mn_2O_3/SMO display significant peak shifts to higher binding energy in O *1s* and to lower binding energy in Mn *2p* under both NO and NO + O_2 atmospheres at 200 and 300 °C (Supplementary Fig. 21). In comparison, the SMO shows trivial changes in NO adsorption and oxidation processes. To further investigate the dynamic changes, we derived the variation curves of the valence state of Mn and O_{latt} content *versus* the reaction conditions by calculating the fitting data of Mn *2p* and O *1s* XPS spectra (Supplementary Figs. 22–41). There is a slight decrease in

the average valence state of Mn (Fig. 3a) and a consequent increase of adsorbed oxygen content (Supplementary Fig. 42) on the SMO surface at 200 °C, however, the lattice oxygen position and O_{latt}/(Sm+Mn) does not change during the process (Fig. 3a and Supplementary Fig. 43). The results suggest that the surface O_{latt} species on SMO have poor reactivity in NO oxidation and that NO gas mainly adsorbs at the SMO surface at low temperature. When O_2 is also introduced at 200 °C, a weak increase in the valence state of Mn is observed, which can be attributed to the partial oxidation of NO and stored on SMO at Mn sites. The position of O_{latt} still fails to respond to NO and O_2 even at 300 °C. The results suggest that traditional Mn sites are only active, the O_{latt} sites of SMO hardly participate in NO adsorption and oxidation reaction below 300 °C. As for Mn_2O_3/SMO, when NO is introduced, the position of O_{latt} slightly shifts to lower binding energy and there is a decrease in the ratio of O_{latt}/O_{ads} and O_{latt}/(Sm+Mn); at the same time, the valence state of Mn also decreases (Fig. 3a). The results indicate that the O_{latt} sites considerably react with NO even at 200 °C, which leads to the electron transfer from NO to Mn via the covalent bond of O_{latt}-Mn^{3+}. When O_2 is also introduced at 200 °C, the valence state of Mn is even higher than that under vacuum conditions (surface oxidation process), and the position of O_{latt} moves back to its original binding energy, suggesting that the reacted O_{latt}-Mn^{3+} groups undergo a regeneration process by the O_2 dissociation at oxygen vacancies (Supplementary Fig. 43).

On increasing the temperature, the reactivity of O_{latt} also increases because of increased changes in NO and NO + O_2 atmospheres. One should note that there is an imbalance between the Mn valence state and the O_{latt} quantity in the regeneration process, namely that Mn in Mn_2O_3/SMO has a higher valence state and O_{latt} has a lower position, whereas the oxidation state of the Mn atoms in SMO increases and the O_{latt} position remains unchanged. This can be due to the enhancement of oxygen adsorption, dissociation, and exchange. At 300 °C, the consumption rate of O_{latt} on Mn_2O_3/SMO is even larger than the compensation rate. The dynamic evolutions from *NAP-XPS* confirm that the O_{latt} sites on Mn_2O_3/SMO act as the primary active sites in NO

oxidation. Moreover, we also directly observed that the surface Sm content (Sm/Mn ratio) in SMO increases when increasing the reaction temperature, whereas the surface Sm content in Mn_2O_3/SMO decreases (Supplementary Fig. 44). Large-ion-radius Sm cations on Mn_2O_3/SMO contribute to preserve its mullite crystal structure and tune the interface interactions, but they are the inactive as metal sites in NO oxidation (Supplementary Figs. 45, 46). Thus, the SMO catalyst shows poor durability during the catalytic oxidation process due to surface Sm enrichment, whereas the Mn_2O_3/SMO catalyst possesses excellent durability owing to surface Mn enrichment.

We further summarize the transfer process of oxygen species on the Mn_2O_3/SMO surface in the cooperative MvK mechanism. Traditional SMO catalysts mainly comply with the E-R mechanism, where adsorbed oxygen species at the Mn sites react with NO gas and are converted into adsorbed nitrates. Differently, for Mn_2O_3/SMO there exists a strong electron transfer between two phases, which efficiently activates the surface O_{latt} sites. Mn_2O_3/SMO has obvious changes in lattice oxygen and adsorbed oxygen species at 300 °C (Fig. 3a and Supplementary Figs. 42, 43). Under a NO atmosphere, NO gas reacts with lattice oxygen into adsorbed nitrate and nitrite species, where lattice oxygen is consumed and are not compensated. The Mn valence state in Mn_2O_3/SMO also has a distinct decrease. When NO and O_2 are introduced, lattice oxygen is dynamically consumed and regenerated. The lattice oxygen position does not restore the original peak position, but the valence state of the Mn atoms has a strong increase (Fig. 3a). These results indicate that the lattice oxygen consumption rate of Mn_2O_3/SMO is faster than regeneration rate at 300 °C. Therefore, Mn_2O_3/SMO complies with the dominated MvK mechanism and to a lesser degree the E-R mechanism. The oxygen transfer process with the Mn_2O_3/SMO catalyst mainly occurs at the Mn sites and oxygen vacancies. Introduction of oxygen makes nitrites and nitrates easily desorbed from the surface due to the oxidative environment.

As a complementary technology to *NAP-XPS* spectra (1–4 nm), *NAP-XAS* spectra usually provide a shallower surface probe depth (1-3 nm in Auger electron yield (AEY) mode). It can be used to identify the chemical descriptors such as covalency of metal-oxygen bond and electron density by examining the electron transition probability at various orbitals under different reaction conditions[49,50]. To monitor the dynamic evolutions on surface electronic structure at O_{latt} and Mn sites, we employed *NAP-XAS* spectra of the O K-edge and Mn L-edge using the total electron yield (TEY) and AEY modes (Supplementary Figs. 47–54), respectively. As known, the AEY mode is more surface-sensitive than the TEY mode, and it includes more detailed covalency information of the metal-oxide bond, while the TEY mode includes information about the O_2 adsorption and electron density of cations[37]. The covalency of the Mn-O bond is confirmed by the peak of Mn 3d-O 2p hybrid orbitals at the O K-edge at around 529 eV and the peak distance (ΔE) for the Mn L_3-edge in 641–644 eV. In the AEY mode, the covalency of the Mn-O bond on SMO (Fig. 3b) is inactive under both reduced and oxidized atmospheres. In contrast, Mn_2O_3/SMO exhibits a distinct enhancement in the covalency of the Mn-O bond under a reduced atmosphere, and an additional shoulder peak in the Mn L_3-edge spectra at around 640 eV occurred (Supplementary Fig. 52). The results suggest that surface O_{latt} shows high activity in the process of bonding with H^* radicals and reduction of Mn sites, leading to the increase of Mn 3d empty orbitals. When O_2 was introduced, it could adsorb at Mn sites and partially heal the oxygen vacancies at 150 °C, resulting in the decrease of covalency of the Mn-O bond. One should note that the position of O_{latt} under a H_2 atmosphere at 300 °C is still lower than that at 150 °C, which can be due to the influence of temperature on the O_{latt} migration. Under oxidized conditions at 300 °C, O_2 can almost fill nearly all the oxygen vacancies, restoring the pristine covalency of the Mn-O bond under vacuum.

The TEY mode of O K-edge and Mn L-edge *XAS* spectra is used to describe the O_2 adsorption and electron density (Fig. 3c). The O_2 adsorption intensity is calculated using the peak intensity ratios of the first two peaks, α and β, in the O K-edge *XAS* spectra, while the electron density is calculated using the peak intensity ratios of two peaks, A and B, in the Mn L_3-edge. The electron density of SMO at the Mn sites slightly changes under redox cycles, while O_2 can adsorb and dissociate at the Mn sites of SMO, leading to a decrease in the electron density of the Mn sites. Whereas Mn_2O_3/SMO exhibits a considerable increase in electron density of Mn sites under an H_2 atmosphere, especially at 150 °C, and the behavior of O_2 adsorption and electron density of Mn sites under O_2 atmosphere at 300 °C are similar to SMO. The results suggest that the Mn sites of Mn_2O_3/SMO are still less active at 300 °C, consistent with the H_2-TPR results. The time-resolved MS signals of H_2O also confirm the redox cycles (Supplementary Fig. 55). It is found that the active sites on Mn_2O_3/SMO are dominated by O_{latt} sites, whereas on SMO, it is the traditional Mn sites. The active order shows accordance with that in NO oxidation at 150 and 300 °C. The above *NAP-XPS* and *NAP-XAS* results directly demonstrate the temperature-dependent changes in the valence state of Mn and the covalence of the Mn-O bond and further validate the roles of O_{latt} at the interface between exsolved-Mn_2O_3 and mullite support.

Key intermediate species in NO oxidation

To gain insights into intermediates in NO oxidation, in-situ diffuse reflectance infrared Fourier transformations spectroscopy (DRIFTS) spectra were recorded for Mn_2O_3/SMO and SMO under NO and NO + O_2 conditions (Fig. 4a–c and Supplementary Fig. 56). The peak intensity of the IR spectra was converted into Kubelka-Munk units to analyze the concentration variations of intermediates. The observed bands at 1235, 1270, and 1570 cm^{-1} correspond to the bridged, monodentate, and bidentate nitrate species, respectively[16,17]. In addition, the band at 1615 cm^{-1} is assigned to the weakly adsorbed NO_2 at O_{latt} sites (O_{latt}-NO_2) as the nitrite species[5,10]. Mn_2O_3/SMO exhibits a stronger IR peak signal for nitrate species compared to SMO under NO + O_2 at 200 °C (Fig. 4a), indicating the superior NO adsorption ability of Mn_2O_3/SMO. Mn_2O_3/SMO possesses more monodentate nitrates than SMO. In addition, we observed an increase in the amount of adsorbed NO_2 (1615 cm^{-1}, nitrite species) at active O_{latt} sites of Mn_2O_3/SMO. Desorption of nitrites and monodentate nitrates to NO_2 is known to be more facile than the bridged nitrate[17]. Mn_2O_3/SMO exhibits rapid NO oxidation activation on the surface due to the larger peak intensity variations compared to SMO (Fig. 4b-c). When O_2 is introduced, the amount of monodentate nitrate in Mn_2O_3/SMO distinctly decreases and the bidentate and bridged nitrate species show slight decreases. However, the adsorbed NO_2 at O_{latt} sites (nitrite species) of Mn_2O_3/SMO increased[17,34]. The result demonstrates the transformation from the nitrates to nitrites during oxygen-rich NO oxidation.

The N 1s *NAP-XPS* spectra (Supplementary Figs. 57, 58) confirm that NO gas preferred to adsorb at the O_{latt} sites of Mn_2O_3/SMO, and its intermediates contain extra O_{site}-NO and O_{site}-NO_2 species compared to traditional SMO. The adsorbed NO on O_{latt} can transform into nitrite species and oxygen vacancy (-O_{latt}-NO_2-Mn-O_v), and the chemical bond for O_{latt}-N can be broken into NO_2. The SMO catalyst mainly complies with the E-R mechanism, where adsorbed oxygen species react with NO gas into nitrate species, such as monodentate, bidentate, bridged nitrates. Different from SMO, Mn_2O_3/SMO depends on the dominated MvK mechanism and to a lesser extent the E-R mechanism. NO gas preferentially adsorbs on lattice oxygen sites and produces the extra nitrite species (O_{site}-NO_2). The nitrites on the lattice oxygen can more easily desorb from the catalyst surface compared to traditional nitrate species. These results highlight that the higher NO oxidation activity of Mn_2O_3/SMO stems from the quick decomposition or desorbed process of nitrite species and monodentate nitrates to NO_2.

To clarify the water effect mechanism on mullite oxides in NO oxidation, we investigated in-situ DRIFTS spectra under the atmosphere of NO + O_2 + H_2O at 200 °C (Supplementary Fig. 59). The
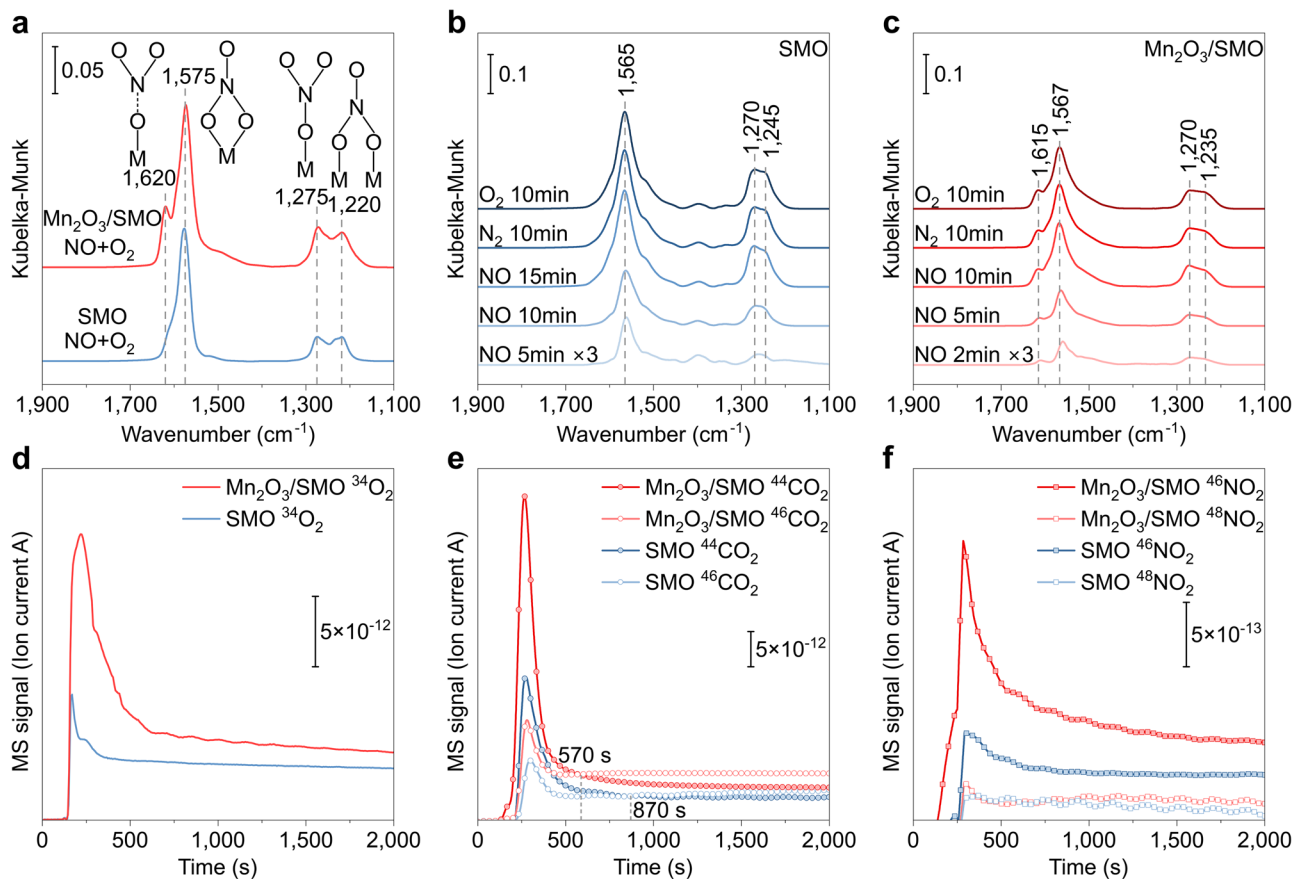
Fig. 4 | Active sites and reaction mechanisms in NO oxidation. a In-situ diffuse reflectance infrared Fourier transform spectroscopy (DRIFTS) of $Mn_2O_3/SmMn_2O_5$ (Mn_2O_3/SMO) and $SmMn_2O_5$ (SMO) under NO + O_2 at 200 °C. Time-resolved in-situ DRIFTS spectra of the (**b**) SMO and (**c**) Mn_2O_3/SMO under NO gas at 200 °C. **d** Time-resolved isotopic $^{36}O_2$ exchange reaction at 300 °C, (**e**) time-resolved isotopic $^{36}O_2$ labeled online MS for CO oxidation at 150 °C, (**f**) time-resolved isotopic $^{36}O_2$ labeled online MS for NO oxidation at 300 °C.

intermediates formed over the SMO and Mn_2O_3/SMO catalysts are described in Supplementary Table 2. The IR vibration intensity of water over the SMO catalyst (water at 1625 cm^{-1} and hydroxyl in 3400–3700 cm^{-1}) is far stronger than that over Mn_2O_3/SMO (1647 cm^{-1} and 3400–3700 cm^{-1}), indicating that the SMO surface is covered by water molecules and a stronger competitive adsorption exists with reactant gases than does for Mn_2O_3/SMO (Supplementary Fig. 59). The IR peak at 1625 cm^{-1} can be attributed to absorbed nitrite species (Supplementary Table 2). If it is nitrite species, this will confirm that water is mainly adsorbed at the Mn active sites of the SMO catalyst and the competitive adsorption makes the NO oxidation comply more with the MvK mechanism at the O_{latt} sites. Therefore, the water poisoning mainly originates from the competitive adsorption and the desorbed NO_3^- species binding with water. The observed monodentate nitrate and nitrite species demonstrate the E-R mechanism at the Mn site and cooperative MvK mechanism at O_{latt} site in NO oxidation, respectively. These two reaction mechanisms are negatively affected by water vapor through the competitive adsorption and desorbed nitrates.

DFT calculations were conducted to further elucidate the impacts of O_{latt} sites in NO oxidation and NO_2 desorption (Supplementary Fig. 60). The models are constructed based on the experimental results and previous reports[10,27,33]. The O-Mn^{4+} of the SMO model exhibits a higher energy barrier of 2.79 eV in NO oxidation (E1) at the O_{latt} sites. However, the O-Mn^{3+} of the SMO model in E1 is lower (1.45 eV), whereas the O-Mn^{3+} of the Mn_2O_3/SMO model is even lower at 0.56 eV. The results confirm that O-Mn^{3+} of Mn_2O_3/SMO is the major active site in NO oxidation. Oxygen vacancy formation energies of

interface Mn^{3+}-O_{site} in Mn_2O_3/SMO, Mn^{3+}-O_{site} in SMO, and Mn^{4+}-O_{site} in SMO also agree with the above calculations, where they are ~1.1 eV, ~1.8 eV and ~2.7 eV, respectively. In addition, the NO_2 desorption (O_{latt}-NO_2 species) on the O-Mn^{3+} of Mn_2O_3/SMO and SMO are exothermic processes (−0.68 and −0.50 eV), while it is an endothermic process (0.11 eV) on the O-Mn^{4+} of SMO. The results indicate that NO_2 is more easily desorbed from the O-Mn^{3+} sites, which is aligned well with the in-situ spectroscopy results.

The time-resolved isotopic $^{36}O_2$ exchange experiments are measured to demonstrate the activity of lattice oxygen (Fig. 4d). Each sample was pretreated at 300 °C for 3 h under an Ar atmosphere to decrease surface adsorbed oxygen. It was revealed that Mn_2O_3/SMO exhibits higher O_{latt} activation and dissociation abilities compared to SMO because of the stronger $^{34}O_2$ signals of Mn_2O_3/SMO *versus* those of SMO. To investigate the activity of O_{latt} sites, we use CO and isotopic $^{36}O_2$ as the probe molecules at 150 °C. To further investigate the activation and dissociation ability of molecular oxygen, the transient oxygen exchange test was conducted at different temperatures. Wachsman et al. proposed that the exchange of lattice oxygen ($^{34}O_2$) on non-stoichiometric metal oxides is usually better at oxygen dissociation when using 1:1 isotopic mixture[51,52]. By analyzing the concentration variations of oxygen exchange (Supplementary Figs. 61, 62), we demonstrate that the oxygen exchange rate of Mn_2O_3/SMO is distinctly higher than that of SMO at the same temperature. At 300 °C, the Mn_2O_3/SMO shows the better oxygen activation ability, while the oxygen exchange rate of SMO is very low. The results are consistent with the *NAP-XPS* spectra and previous work on perovskites[51,52].

Furthermore, we also calculated the apparent activation energy of O_2 for the two catalysts by the slope of Arrhenius plot. The apparent oxygen activation energy of SMO and Mn_2O_3/SMO catalysts are 38.8 and 44.8 kJ/mol, respectively.

Both the MvK and E-R mechanisms exist in the Mn_2O_3/SMO catalyst (Fig. 4e), as indicated by the simultaneous appearance of $^{44}CO_2$ and $^{46}CO_2$ signals. Interestingly, Mn_2O_3/SMO exhibits an earlier crossing time (570 s) in the $^{44}CO_2$ and $^{46}CO_2$ signals compared to SMO (870 s), with a stronger initial intensity of $^{44}CO_2$. This suggests that the consumption rate of O_{latt} with CO in Mn_2O_3/SMO is much higher than that in SMO. On decreasing the temperature to 100 °C (Supplementary Fig. 63), the O_{latt} activity in Mn_2O_3/SMO weakens, and no crossing point is observed during the 2400 s. However, the signal of $^{44}CO_2$ is still stronger than that of $^{46}CO_2$. Therefore, the CO oxidation on Mn_2O_3/SMO mainly follows the MvK mechanism and O_{latt} is the important active site. Furthermore, the time-resolved isotopic $^{36}O_2$ signal at 300 °C (Fig. 4f) shows that the Mn_2O_3/SMO exhibits a much stronger $^{46}NO_2$ signal compared to SMO, while the intensities of $^{48}NO_2$ signal are nearly the same, indicating that the reaction rate at the Mn sites of Mn_2O_3/SMO is low and similar to that of SMO (the E-R mechanism). In contrast, the reaction rate at the O_{latt} sites is significantly improved on Mn_2O_3/SMO, and the NO oxidation pathway is determined by the MvK mechanism.

The reaction orders of Mn_2O_3/SMO and SMO were calculated to achieve strict kinetic control (Supplementary Table 3). The reaction orders of SMO for NO and O_2 are 0.61 and 0.59, respectively, while a noticeable decrease of Mn_2O_3/SMO is observed (0.55 to NO and 0.47 to O_2). As known, lower reaction orders to O_2 typically indicate that adsorbed oxygen can be easily activated at a catalyst surface with oxygen vacancies[53]. That is, decomposition of O_2 is more facile at the surface of Mn_2O_3/SMO. In addition, the decrease in NO reaction orders can be attributed to the strong competitive adsorption of O_2 to NO. As demonstrated through in-situ spectroscopy results, the Mn_2O_3/SMO catalyst presents both higher covalency of Mn−O bond and electron density of Mn sites, which leads to the generation of more O_{latt} sites. These O_{latt} sites facilitate the activities of NO oxidation dominated by the cooperative MvK mechanism.

Discussion

We have prepared a highly active DOC catalyst whereby Mn_2O_3 is exsolved from mullite surface by a facile nonstoichiometric exsolution method. By a series of in-situ spectroscopies, we elucidate the role and dynamic evolutions of lattice oxygen, serving as the predominant active sites, in NO oxidation. Different from the traditional mullite catalyst, lattice oxygen adjacent to Mn^{3+} cations at the interface between exsolved-Mn_2O_3 and the support displays strong covalency of Mn-O bond and electron enrichment at the Mn sites. In both model reactions under redox cycles and NO oxidations, these O_{latt} sites are largely involved in these reactions, exhibiting more significant changes in the valence state of Mn and covalency of the Mn-O bond. Compared to the Eley-Rideal mechanism on the Mn^{4+} cations of mullite, this catalyst follows the characteristic of cooperative Mars-van Krevelen mechanism operating at lattice oxygen sites. The enhanced reaction rates are owing to the lower energy barriers of NO oxidation with lattice oxygen (monodentate nitrates and nitrites) and an exothermic process of NO_2 desorption from the surface. Moreover, the leaving oxygen vacancies can be easily healed by O_2 dissociation to form new O_{latt} sites. Due to the ultra-stable mullite framework and the completion of MnO_x phase transition process at 800 °C (Mn_2O_3 yield), the Mn_2O_3/SMO shows higher activity in NO oxidation (93% at 270 °C), surpassing previously reported Pt-based and mullite-based catalysts (86% at 290 °C and 83% at 300 °C). In addition, it also exhibits an excellent DOC performance under the environment of 8% CO_2 and 8% H_2O. After 50 h hydrothermal aging at 750 °C with a 10% H_2O concentration, the aged Mn_2O_3/SMO catalyst still retains 62.6% conversion for NO and 100% conversions for CO and C_3H_6 at 325 °C.

This work underlines three pivotal factors in understanding the roles of O_{latt} sites: (1) the electron exchanges between exsolved-Mn_2O_3 and mullite support, resulting in the formation of more active O_{latt}-Mn^{3+} local structures, (2) the incorporation of hybrid orbitals of Mn $3d$ and O $2p$, which amplifies the covalency of the Mn−O bond, and (3) the interface and defect induced lattice contractions on the mullite support. These findings advance our comprehension of lattice oxygen behavior, forging a new avenue in the design of metal-oxide-based catalysts. This work will push the frontiers of academic research and the practical applications in the heterogeneous catalysis realm.

Methods

Experiment and Methods are shown in the Supplementary Information.

Data availability

Source data are provided with this paper. The authors declare that the data supporting the findings of this study are available within the paper, its supplementary information files, and the Figshare repository. Source data are provided with this paper.

References

1. Anenberg, S. C. et al. Impacts and mitigation of excess diesel-related NO_x emissions in 11 major vehicle markets. *Nature* **545**, 467–471 (2017).
2. Wang, W. et al. Mixed-phase oxide catalyst based on Mn-mullite (Sm, Gd)Mn_2O_5 for NO oxidation in diesel exhaust. *Science* **337**, 832–835 (2012).
3. Kim, C. H., Qi, G., Dahlberg, K. & Li, W. Strontium-doped perovskites rival platinum catalysts for treating NO_x in simulated diesel exhaust. *Science* **327**, 1624–1627 (2010).
4. Hoang, S. et al. Activating low-temperature diesel oxidation by single-atom Pt on TiO_2 nanowire array. *Nat. Commun.* **11**, 1062 (2020).
5. Wang, F. et al. Ultralow-temperature NO_x reduction over $SmMn_2O_5$ mullite catalysts via modulating the superficial dual-functional active sites. *ACS Catal.* **12**, 7622–7632 (2022).
6. Russell, A. & Epling, W. S. Diesel oxidation catalysts. *Catal. Rev.* **53**, 337–423 (2011).
7. Kothari, M. et al. Platinum incorporation into titanate perovskites to deliver emergent active and stable platinum nanoparticles. *Nat. Chem.* **13**, 677–682 (2021).
8. Nie, L. et al. Activation of surface lattice oxygen in single-atom Pt/CeO_2 for low-temperature CO oxidation. *Science* **358**, 1419–1423 (2017).
9. Kunwar, D. et al. Investigating anomalous growth of platinum particles during accelerated aging of diesel oxidation catalysts. *Appl. Catal. B* **266**, 118598 (2020).
10. Zheng, Y. et al. Stable and active oxidation catalysis by cooperative lattice oxygen redox on $SmMn_2O_5$ mullite surface. *J. Am. Chem. Soc.* **141**, 10722–10728 (2019).
11. Ulissi, Z. W., Medford, A. J., Bligaard, T. & Nørskov, J. K. To address surface reaction network complexity using scaling relations machine learning and DFT calculations. *Nat. Commun.* **8**, 14621 (2017).
12. Medford, A. J. et al. From the Sabatier principle to a predictive theory of transition-metal heterogeneous catalysis. *J. Catal.* **328**, 36–42 (2015).
13. Schlögl, R. Heterogeneous catalysis. *Angew. Chem. Int. Ed.* **54**, 3465–3520 (2015).
14. Shen, Y., Deng, J., Han, L., Ren, W. & Zhang, D. Low-temperature combustion of toluene over Cu-doped $SmMn_2O_5$ mullite catalysts

via creating highly active Cu^{2+}-O-Mn^{4+} sites. *Environ. Sci. Technol.* **56**, 10433–10441 (2022).

15. Simbock, J. et al. Electronic parameters in cobalt-based perovskite-type oxides as descriptors for chemocatalytic reactions. *Nat. Commun.* **11**, 652 (2020).

16. Yang, Q. et al. Surface tailoring on $SrMnO_3$@$SmMn_2O_5$ for boosting the performance in diesel oxidation catalyst. *Appl. Catal. B* **320**, 121993 (2023).

17. Yang, Q. et al. Surface Reconstruction of a mullite-type catalyst via selective dissolution for NO oxidation. *ACS Catal.* **11**, 14507–14520 (2021).

18. Meng, F. et al. Essential role of lattice oxygen in methanol electrochemical refinery toward formate. *Sci. Adv.* **9**, eadh9487 (2023).

19. Jacobs, R., Mayeshiba, T., Booske, J. & Morgan, D. Material discovery and design principles for stable, high activity perovskite cathodes for solid oxide fuel cells. *Adv. Energy Mater.* **8**, 1702708 (2018).

20. Mueller, D. N., Machala, M. L., Bluhm, H. & Chueh, W. C. Redox activity of surface oxygen anions in oxygen-deficient perovskite oxides during electrochemical reactions. *Nat. Commun.* **6**, 6097 (2015).

21. Grimaud, A. et al. Activation of surface oxygen sites on an iridium-based model catalyst for the oxygen evolution reaction. *Nat. Energy* **2**, 16189 (2016).

22. Grimaud, A. et al. Activating lattice oxygen redox reactions in metal oxides to catalyse oxygen evolution. *Nat. Chem.* **9**, 457–465 (2017).

23. Hwang, J. et al. Perovskites in catalysis and electrocatalysis. *Science* **358**, 751–756 (2017).

24. Pearce, P. E. et al. Evidence for anionic redox activity in a tridimensional-ordered Li-rich positive electrode beta-Li_2IrO_3. *Nat. Mater.* **16**, 580–586 (2017).

25. Assat, G. & Tarascon, J.-M. Fundamental understanding and practical challenges of anionic redox activity in Li-ion batteries. *Nat. Energy* **3**, 373–386 (2018).

26. McCalla, E. et al. Understanding the roles of anionic redox and oxygen release during electrochemical cycling of lithium-rich layered Li_4FeSbO_6. *J. Am. Chem. Soc.* **137**, 4804–4814 (2015).

27. Zhang, T. et al. Electrospun YMn_2O_5 nanofibers: A highly catalytic activity for NO oxidation. *Appl. Catal. B* **247**, 133–141 (2019).

28. Thampy, S. et al. Role of surface oxygen vacancies in intermediate formation on mullite-type oxides upon NO adsorption. *J. Phys. Chem. C.* **124**, 15913–15919 (2020).

29. Zhang, T. et al. Promotion of low-temperature oxidation of propane through introduction of Ce into mullite oxide YMn_2O_5. *ChemPlusChem* **87**, e202100455 (2022).

30. Thampy, S. et al. Superior low-temperature NO catalytic performance of $PrMn_2O_5$ over $SmMn_2O_5$ mullite-type catalysts. *Catal. Sci. Techn.* **9**, 2758–2766 (2019).

31. Thampy, S., Ashburn, N., Cho, K. & Hsu, J. W. P. Earth-abundant transition metal-based mullite-type oxide catalysts for heterogeneous oxidation reactions. *Adv. Energy Sustain. Res* **2**, 2000075 (2021).

32. Chen, Z., Liu, X., Cho, K., Chen, R. & Shan, B. Density functional theory study of the oxygen chemistry and NO oxidation mechanism on low-index surfaces of $SmMn_2O_5$ mullite. *ACS Catal.* **5**, 4913–4926 (2015).

33. Yang, J. et al. Origin of the superior activity of surface doped $SmMn_2O_5$ mullites for NO oxidation: a first-principles based microkinetic study. *J. Catal.* **359**, 122–129 (2018).

34. Hwang, J. et al. Regulating oxygen activity of perovskites to promote NO_x oxidation and reduction kinetics. *Nat. Catal.* **4**, 663–673 (2021).

35. Zhu, Y. et al. Fundamental mechanistic insights into the catalytic reactions of Li-S redox by Co single-atom electrocatalysts via operando methods. *Sci. Adv.* **9**, eadi5108 (2023).

36. Qiao, R., Chin, T., Harris, S. J., Yan, S. & Yang, W. Spectroscopic fingerprints of valence and spin states in manganese oxides and fluorides. *Curr. Appl. Phys.* **13**, 544–548 (2013).

37. Long, X. et al. Direct spectroscopy for probing the critical role of partial covalency in oxygen reduction reaction for cobalt-manganese spinel oxides. *Nanomaterials* **9**, 577 (2019).

38. Wang, X. et al. Manipulating surface termination of perovskite manganate for oxygen activation. *Adv. Funct. Mater.* **31**, 2006439 (2021).

39. Li, L., Shen, Q., Cheng, J. & Hao, Z. Catalytic oxidation of NO over TiO_2 supported platinum clusters I. Preparation, characterization and catalytic properties. *Appl. Catal. B* **93**, 259–266 (2010).

40. Li, L., Qu, L., Cheng, J., Li, J. & Hao, Z. Oxidation of nitric oxide to nitrogen dioxide over Ru catalysts. *Appl. Catal. B* **88**, 224–231 (2009).

41. Auvray, X. & Olsson, L. Stability and activity of Pd-, Pt- and Pd-Pt catalysts supported on alumina for NO oxidation. *Appl. Catal. B* **168**, 342–352 (2015).

42. Adjimi, S. et al. Highly efficient and stable Ru/K-OMS-2 catalyst for NO oxidation. *Appl. Catal. B* **219**, 459–466 (2017).

43. Jeong, H. et al. Controlling the oxidation state of Pt single atoms for maximizing catalytic activity. *Angew. Chem. Int. Ed.* **59**, 20691–20696 (2020).

44. Liu, S., Wu, X., Weng, D., Li, M. & Lee, H.-R. Combined promoting effects of platinum and MnO_x-CeO_2 supported on alumina on NO_x-assisted soot oxidation: thermal stability and sulfur resistance. *Chem. Eng. J.* **203**, 25–35 (2012).

45. Ogel, E. et al. Impact of preparation method and hydrothermal aging on particle size distribution of Pt/γ-Al_2O_3 and its performance in CO and NO. *Oxid. J. Phys. Chem. C.* **123**, 5433–5446 (2019).

46. Wen, Y., Zhang, C., He, H., Yu, Y. & Teraoka, Y. Catalytic oxidation of nitrogen monoxide over $La_{1-x}Ce_xCoO_3$ perovskites. *Catal. Today* **126**, 400–405 (2007).

47. Thampy, S. et al. Superior catalytic performance of Mn-mullite over Mn-perovskite for NO oxidation. *Catal. Today* **310**, 195–201 (2018).

48. Datye, A. & Votsmeier, M. Opportunities and challenges in the development of advanced materials for emission control catalysts. *Nat. Mater.* **20**, 1049–1059 (2021).

49. Mueller, D. N. Data collection strategies, analysis, and interpretation in AP-XAS. in *Ambient Pressure Spectroscopy in Complex Chemical Environments*, 315–331 (American Chemical Society, 2021).

50. Zhang, H. et al. Ambient pressure mapping of resonant Auger spectroscopy at BL02B01 at the Shanghai Synchrotron Radiation Facility. *Rev. Sci. Instrum.* **91**, 123108 (2020).

51. Huang, Y., Pellegrinelli, C. & Wachsman, E. D. Direct observation of oxygen dissociation on non-stoichiometric metal oxide catalysts. *Angew. Chem. Int. Ed.* **55**, 15268–15271 (2016).

52. Huang, Y., Pellegrinelli, C. & Wachsman, E. D. Reaction kinetics of gas-solid exchange using gas phase isotopic oxygen exchange. *ACS Catal.* **6**, 6025–6032 (2016).

53. Lu, Y. et al. Identification of the active complex for CO oxidation over single-atom Ir-on-$MgAl_2O_4$ catalysts. *Nat. Catal.* **2**, 149–156 (2018).

Acknowledgements

Author contributions

All authors contributed to the discussion and approved the manuscript. These authors contributed equally to this work: X.W. and Q.Y. Methodology: X.W., Q.Y., Y.P. Investigation and synthesis: X.W., Q.Y. Characterizations: X.W., Q.Y., X.L., C.G., Z.L., H.Z., S.S., X.C. Supervision: X.W., Y.P. Writing—original draft: X.W., Q.Y., Y.P. Writing—review & editing: X.W., Y.W., Y.M., C.R., Y.P., J.L., S.F.

Competing interests

The authors declare no competing interests.

Additional information

Supplementary information The online version contains supplementary material available at
https://doi.org/10.1038/s41467-024-51473-9.

Correspondence and requests for materials should be addressed to Yue Peng.

Peer review information *Nature Communications* thanks Rong Chen and the other, anonymous, reviewers for their contribution to the peer review of this work. A peer review file is available.

Reprints and permissions information is available at
http://www.nature.com/reprints

Publisher's note Springer Nature remains neutral with regard to jurisdictional claims in published maps and institutional affiliations.